Inorganic Chemistry Communications 179 (2025) 114887

Contents lists available at ScienceDirect

Inorganic Chemistry Communications

journal homepage: www.elsevier.com/locate/inoche

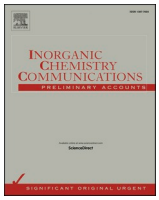

Short communication

Copper pincer targets SARS-CoV-2 Omicron, Delta, and Wild-Type receptor binding domains☆

Matthew L. Bracken [a,*], Thandeka Moyo-Gwete [b], Sheldon Sookai [a,*], Frances Ayres [b], Orde Q. Munro [a,c]

[a] University of the Witwatersrand, Molecular Sciences Institute, South Africa
[b] The National Institute for Communicable Diseases of South Africa, South Africa
[c] University of Leeds, Department of Chemistry, United Kingdom

ARTICLE INFO

Keywords:
Copper
Pincer ligands
Covid
SARS
Therapeutic
Fluorescence

ABSTRACT

A novel copper(II) pincer was synthesized and crystallized to form a metallocycle hexamer. The metal chelate was designed to target solvent-exposed amino acid residues on the SARS-CoV-2 spike protein with the potential to act as a chemotherapeutic agent in the treatment of COVID-19.

1. Introduction

On December 31, 2019, the World Health Organization (WHO) detected reports from Wuhan, China, of a novel "viral pneumonia". Within two weeks, the first death was recorded, and the genetic sequence of the RNA virus was published. By March 11, 2020, the WHO declared severe acute respiratory syndrome coronavirus 2 (SARS-CoV-2) a Public Health Emergency of International Concern, marking the onset of a global pandemic [1]. The virus spread rapidly, overwhelming healthcare systems, collapsing economies, and causing unprecedented mortality due to respiratory failure. In four years, over 775 million infections and 7 million deaths were recorded [2], with global life expectancy declining due to 28 million excess years of life lost in 2020 [3]. This massive death toll may have been reduced had broad-spectrum antiviral agents already been approved for medical use.

SARS-CoV-2 is an enveloped virus, the genome of which encodes four main structural proteins and 16 non-structural proteins (NSP), all of which are potential drug targets [4]. The most recognizable structural protein of the coronavirus (CoV) is the spike (S), which is an ectodomain homotrimeric glycoprotein where each S protein monomer consists of two subunits, S1 and S2. The S1 subunit contains the receptor-binding domain (RBD), which interacts with human ACE2, facilitating viral entry [5,6]. The ACE2 receptor is bound at the peptidase domain which contains an α-helical coil that serves as a binding site when cradled within the concave receptor binding motif of the S protein. The bridge that forms when ACE2 is flanked against the RBD involves key interactions with 17 protein residues including four tyrosine residues (Y449, Y453, Y489, and Y505 [6], which correspond to four tyrosine residues (Y436, Y440, Y475, and Y491) on SARS-CoV. This underscore the evolutionary conservation of ACE2 binding mechanisms [6]. The pandemic witnessed the emergence of new SARS-CoV-2 variants such as Delta [7], and Omicron [8], predominantly harbouring mutations in the S protein. While these mutations raised concerns about therapeutic targeting, the conserved tyrosine residues remained crucial for ACE2 recognition. The crystal structures of SARS-CoV-2 wild-type (WT) [6], Delta [7], Omicron [8], and SARS-CoV [9] RBD bound to ACE2 are presented in Fig. S4.1. The structural alignment of WT, Delta, and Omicron RBDs has 99 % sequence identity and an RMSD of 0.72 Å. The tyrosine residues involved with ACE2 receptor recognition are identical for WT and Delta variants. The Omicron variant harbours the Y505H mutation as well as the N501Y mutation; the newly emerged Y501 is still involved in ACE2 recognition.

Future coronavirus outbreaks are inevitable [10]. To counteract them, we propose the design of novel metal pincers that selectively bind

☆ *Electronic Supplementary Information (ESI) available: Complete experimental details and supplementary tables and figures in PDF format, X-ray crystal structure in CIF format (CCDC 2356073).*

* Corresponding authors.
E-mail addresses: matthewbracken125@gmail.com (M.L. Bracken), Sheldon.Sookai@wits.ac.za (S. Sookai).

https://doi.org/10.1016/j.inoche.2025.114887
Received 7 February 2025; Received in revised form 28 May 2025; Accepted 11 June 2025
Available online 14 June 2025

solvent-exposed tyrosine residues on the RBD, acting as broad-spectrum fusion inhibitors. By disrupting critical ACE2-RBD interactions, these inhibitors could prevent viral entry and fusion, providing a strategic approach for pandemic preparedness. Figs. S4.1-S4.3 illustrate the structural insights guiding our design. This approach offers a promising avenue for antiviral development, ensuring readiness for future coronavirus threats.

Already, fusion inhibitors involving therapeutic antibodies [11] and lipopeptides [12,13] have been shown to inhibit SARS-CoV-2 replication *in vitro*. Our strategy was to design metal pincers with bioavailable metal ions such as copper, which has been shown to avidly bind tyrosine [14,15]. In our opinion, a Cu(II)-based metal pincer will serve as a viable option for the development of a universal fusion inhibitor that targets solvent-exposed tyrosine residues on the CoV RBD.

Cu1 (Fig. 1a) was synthesized (S2) and docked against Y449, Y453, Y489, and Y505 of WT RBD (Fig. 1b) to show that targeting any one of these residues is likely to disrupt ACE2 receptor recognition. **Cu1** was observed to bind tyrosine on a synthetic hexapeptide epitope GVGYQP corresponding to G502-V503-G504-Y505-Q506-P507 on the WT RBD (Fig. 1c, S5.1-S5.3), indicating the copper chelates affinity for O-donor

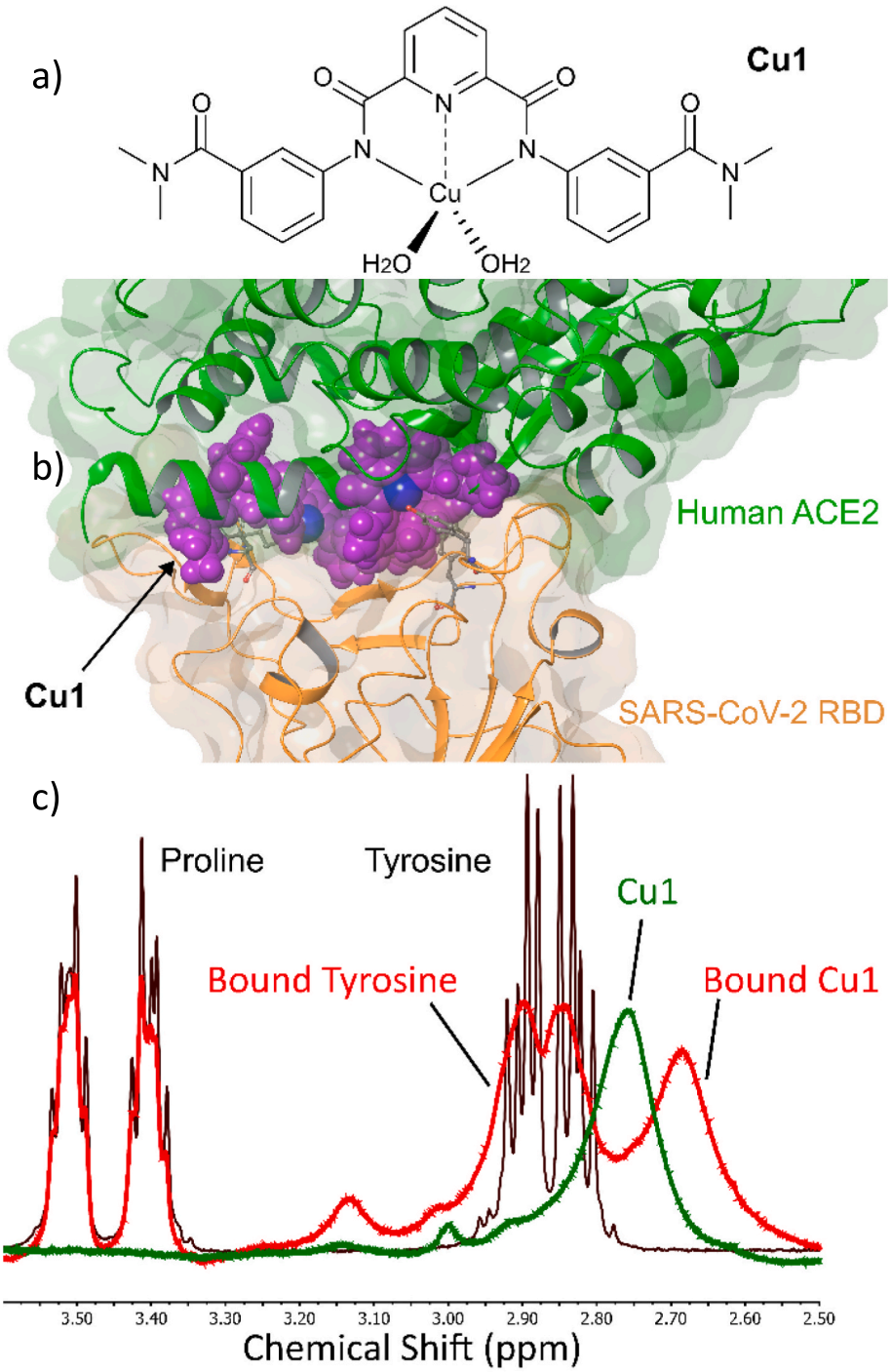

Fig. 1. (a) The structure of Cu1 (b) View of Cu1 docked at Y449, Y453, Y489, and Y505 of the WT RBD (PDB: 2AJF) [6]. (c) The Cu-chelate was shown by ^{1}H NMR (500 MHz in D_2O at 296 K) to bind tyrosine on the synthetic peptide (N–GVGYQP–C) corresponding to Y505 of SARS-CoV-2. Cu1 was reacted with the peptide (0.5:1 ratio) ratio was chosen to balance signal detectability while minimizing excessive broadening.

ligands. The binding affinity between **Cu1** and biomimetic models, *p*-cresol and the hexapeptide epitope, were determined by fluorescence spectroscopy. The binding event between **Cu1** and WT, Delta, and Omicron RBD's was also quantified, and relevant Stern-Volmer parameters [16], such as the biomolecular rate constant (k_q, [17–19]), are presented in Table S1 (Fig. S7.1). The thermodynamics of **Cu1** binding WT, Delta, and Omicron RBD's are presented in Table 1. Recombinant proteins were expressed in HEK 293F cells and purified using affinity- and size-exclusion chromatography prior to biophysical assays (Figs. S3.1-S3.4). Fluorescence quenching of WT RBD in the presence of **Cu1** is presented in Fig. 2a with the Stern-Volmer (SV) plots [16]. The observed downward curvature (Fig. 2b) indicates that the tryptophan fluorophores, W353 and W436, are inaccessible to the **Cu1** quencher (Figs. S7.1–7.3). This eliminates any binding site within 15 – 20 Å of either tryptophan [20].

Hence, binding sites that extend beyond 20 Å of the heteroaromatic fluorophore have been shown in Fig. 2b to include regions close to Cys391-Cys525, Cys480-Cys488, as well as Y449, Y489, Y505, and E484 (Figs. S4.4-S4.5). **Cu1** cannot be bound to Y453 because this residue is sufficiently close to W353 to cause quenching, and Y453 is less solvent-exposed than the remaining tyrosine's making it less accessible to **Cu1**. Therefore, the SV plot shows linearity when tyrosine fluorescence is quenched by **Cu1**, once the binding site has saturated, downward curvature is observed due to tryptophan inaccessibility. Then at high [**Cu1**] a second binding event is observed, possibly a second tyrosine residue.

Hence, binding sites that extend beyond 20 Å of the heteroaromatic fluorophore have been shown in Fig. 2b to include regions close to Cys391-Cys525, Cys480-Cys488, as well as Y449, Y489, Y505, and E484 (Fig. S4.4-S4.5). **Cu1** cannot be bound to Y453 because this residue is sufficiently close to W353 to cause quenching, and Y453 is less solvent-exposed than the remaining tyrosine's making it less accessible to **Cu1**. Therefore, the SV plot shows linearity when tyrosine fluorescence is quenched by **Cu1**, once the binding site has saturated, downward curvature is observed due to tryptophan inaccessibility. Then at high [**Cu1**] a second binding event is observed, possibly a second tyrosine residue.

To delineate the binding site, CD spectroscopy was used to study the interaction between **Cu1** and the SARS-CoV-2 wt, Delta, and Omicron RBD's (Figs. S6.1-S6.6). The perturbation of RBD protein structure in the presence of **Cu1** is shown for the WT variant in Fig. 3. The β-sheet signal at 241 nm responds to increasing [**Cu1**] until an induced signal is observed at *ca.* 500 nm for the protein–ligand complex (Fig. 3a). The tertiary structure fingerprint region [21] between 260 – 320 nm gives insight into the perturbations of aromatic amino acids as well as disulphide bonds. The signal at 260 nm arises from the chirality of disulphide bonds, and significant changes at this wavelength in the presence of **Cu1** indicate that binding occurs near this moiety (Fig. 3b). This implies protein regions close to either Cys391-Cys525 or Cys480-Cys488 are affected by **Cu1** binding. The WT RBD CD spectrum around 270 nm also changes upon titration of **Cu1**, indicating that phenylalanine is affected by the metal complex. There are also significant changes in the CD spectrum between 275 – 280 nm, the region where tyrosine absorption occurs. At a [**Cu1**] of 15 μM the tryptophan signal at 285 nm is unperturbed, indicating that this chromophore is unaffected by **Cu1**. At a

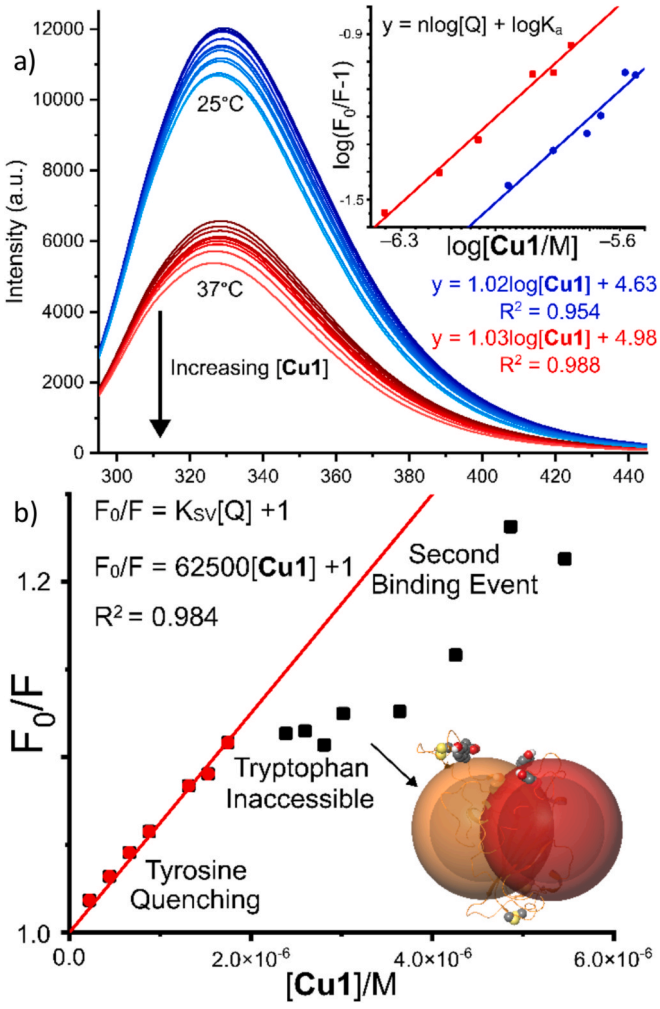

Fig. 2. (a) Emission spectra of WT RBD (0.08 mg/ml) recorded as a function of the concentration of Cu1 at 298 K and 310 K in 3 mM HEPES (pH 7.4, 150 mM NaCl, 0.02 % NaN_3). Insert indicates Double logarithm plot of the fractional change in fluorescence intensity for WT RBD recorded as a function of Cu1 concentration. (b) Stern-Volmer (SV) fluorescence intensity ratio plots for WT RBD recorded as a function of Cu1 concentration of at 298 K. The insert indicates RBD with potential binding sites eliminated 20 Å away from Trp (orange and red spheres). (For interpretation of the references to colour in this figure legend, the reader is referred to the web version of this article.)

[**Cu1**] of 33 μM the signal at 285 nm is affected but is likely due to considerable overlap between Tyr and Trp absorption at longer wavelengths. Hence, due to perturbations of the β-sheet, disulphide bonds, as well as phenylalanine and tyrosine, the **Cu1** binding site is located around Cys480-Cys488. This disulphide bond is shown as yellow space-fill models in Fig. 3a.

Incorporating empirical data from fluorescence and CD spectroscopy

Table 1
The thermodynamic parameters obtained for the binding event between Cu1 and SARS-CoV-2 RBD variants. The standard enthalpies and entropies have been presented along with the Gibbs free energy of binding at 37 °C.

Target	$logK_{SV}$ [a,b]	k_q[17 18 19] × 10^{13}(M^{-1} s^{-1})[a,c]	$logK_a$ [a,d]	n [a,e]	Δ_rG^{Θ} (kJ mol–1)[a]	Δ_rH^{Θ} (kJ mol–1)[a]	Δ_rS^{Θ} (J K–1 mol–1)[a]
WT RBD	4.80 ± 0.02	1.01 ± 0.002	4.98 ± 0.34	1.03 ± 0.06	–29.5 ± 0.4	+51.2 ± 12.6	+260 ± 42
Delta RBD	4.70 ± 0.02	0.810 ± 0.001	4.86 ± 0.24	1.03 ± 0.04	–28.8 ± 0.3	+52.2 ± 8.1	+261 ± 27
Omicron RBD	4.84 ± 0.01	1.11 ± 0.002	4.75 ± 0.38	0.987 ± 0.065	–28.2 ± 0.5	+34.8 ± 7.6	+203 ± 25

[a] The estimated standard deviations of three replicates are given. [b] K_{SV} values (Stern-Volmer constants) were determined from fitting the data to eq. S1. [c] Using eq. S2, a mean excited state lifetime, τ_0, of 5.87(76) ns for Tyr was used to calculate the bimolecular quenching rate constants. [d] Binding affinity was calculated using eq. S3 k_q. [e] Binding stoichiometry.

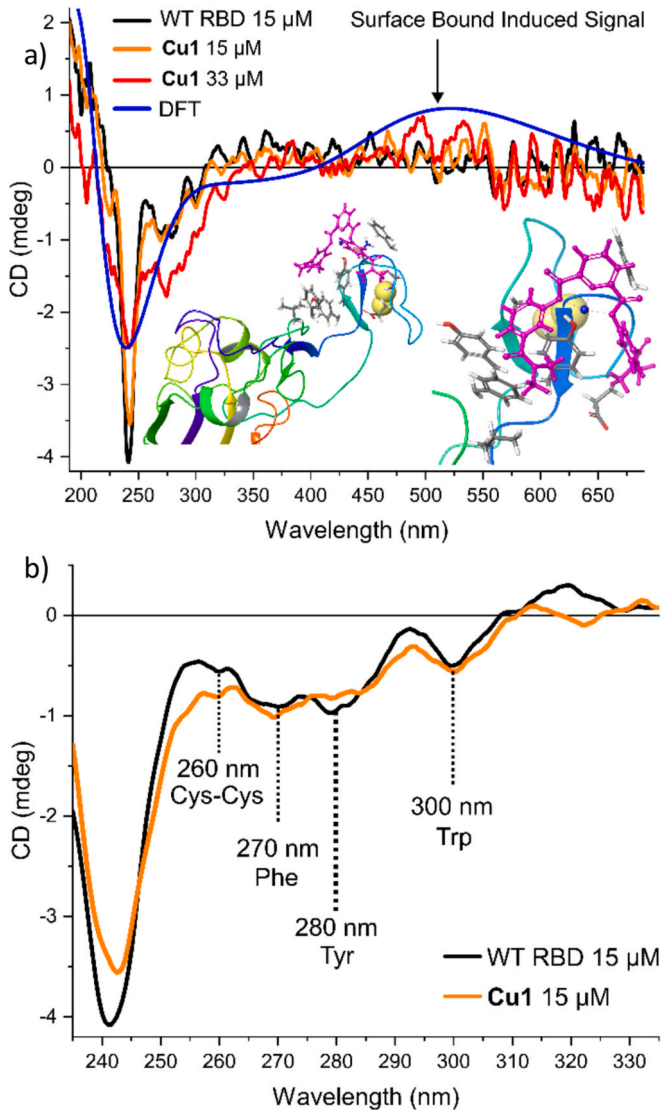

Fig. 3. Comparison of the experimental ICD spectrum recorded for WT RBD• {Cu1} and the CD spectrum calculated using hybrid QM:MM TD-DFT simulations (cam-B3LYP/SDD:UFF) for the top-scoring docked poses of Cu1 bound to Y489 of the WT RBD. (b) Plots of the near UV–visible CD spectra of native WT RBD (15 μM) and the protein incubated with Cu1 (15 μM). The spectra were recorded at 298 K in 3 mM HEPES (pH 7.4, 150 mM NaCl, 0.02 % NaN_3). The aromatic fingerprint region shows significant perturbations at Tyr and Cys-Cys.

into *in silico* docking workflows has been reported [22]. We have adapted this knowledge-based docking workflow to identify the ligand binding site on the RBD target. ONIOM calculations were performed to simulate the experimental CD spectrum and **Cu1** bound to Y489 produced the best correlation as shown in Fig. 3a. Furthermore, a 100 ns MD analysis was performed for **Cu1** bound to E484, Y489, and Y505 (Fig. S4.6). Caveat of **Cu1** binding to the ACE2 receptor is reported in the ESI Fig. S4.6. The results indicate that the **Cu1**-Y489 adduct is most stable in solution over 100 ns. These data are consistent for WT, Delta, and Omicron RBDs, indicating that Y489 is the ligand binding site for all three SARS-CoV-2 variants. A 50 ns MD simulation was performed for the WT RBD-ACE2 protein complex as well as the RBD-ACE2 complex with **Cu1** docked against Y489. The results indicate significant distortion at the RBD-ACE2 interface. Y489 on the RBD maintains contact with Y83 on ACE2 over the 50 ns with a H-bond length of 1.60 Å after equilibration. When **Cu1** is bound, the distance between Y489 and Y83 increases to 16.5 Å after equilibration, indicating that the metal pincer may disrupt receptor recognition and function as a fusion inhibitor (Fig. S4.3). **Cu1** binds WT, Delta, and Omicron RBD variants with a favourable Gibbs free energy close to –30 kJ mol^{-1} at 37 °C and the process is entropically driven for each variant (Table 1). The enthalpic contribution for WT and Delta variants is around + 50 kJ mol^{-1} whilst the ΔH for **Cu1** binding to Omicron is + 35 kJ mol^{-1}.

Although the Omicron binding has a more favourable ΔH, the ΔG remains largely unaffected due to enthalpy–entropy compensation [23], indicating that a single mutation is responsible for the different ΔH and ΔS values observed for Omicron compared to WT and Delta. When **Cu1** is bound at Y489 on WT and Delta variants, the chelate comes into proximity with E484. The Omicron variant harbours the E484G mutation, decreasing the polarity of this binding site. Hence, due to increased polarity of the binding site for WT and Delta variants, the ΔH becomes more positive as work is required to displace water molecules tightly bound to E484 (Fig. S4.7). The enthalpic contribution becomes more favourable for **Cu1** binding Omicron RBD because less work is required to displace water from G484. The coordination environment of the **Cu1** metal centre is the same for WT, Delta, and Omicron variants, because the induced CD signal occurs at *ca.* 500 nm for each binding event, further supporting the claim that Y489 is targeted by **Cu1** (Fig. S6).

It is noted that the phenolic OH group of tyrosine has a pKa of around 10.1 and remains largely protonated at physiological pH. However, From Fig. S3.2 we observe that several Tyr residues are in close proximity to basic amino acids (His, Lys and Arg), this can significantly influence this value. Basic amino acid residues may facilitate partial or transient deprotonation of the OH, enabling coordination to Cu(II) pincer complex. Additionally, the Cu(II) pincer likely engages in non-covalent hydrophobic interactions with tyrosine residues such as π–π stacking, this is corroborated by positive $\Delta_r H^{\ominus}$ and $\Delta_r S^{\ominus}$ values (Table 1). Thus, the observed selectivity likely arises from a combination of weak coordination and secondary interactions stabilized by the local environment.

The solution behaviour of **Cu1** was studied (Figs. S8.1–8.2, Table S2) and the complex was found to be highly water soluble, saturating at 3 mM. The glutathione (GSH) stability of the chelate was tested in MOPS buffer at pH 7.4, and **Cu1** was found to be stable up to 7 eq of GSH under these conditions. The GSH stability was also tested in HEPES buffer at pH 7.4 with 150 mM NaCl which resulted in instant decomposition of **Cu1**. There is also significant demetallation of **Cu1** in PBS (50 mM; pH 7.5; 150 mM NaCl) buffer and 100 % decomposition in 0.01 M $HCl_{(aq)}$. Hence, due to the instability of **Cu1** under biological conditions, live virus data was never collected. However, this limitation does not negate the fundamental findings of our study. Our results provide valuable insights into the binding properties of **Cu1** and its interaction with the RBD under controlled conditions. While *in vivo* applications would require modifications such as changing the metal from Cu^{II} to a different metal ion such as Co^{III}, or Zn^{II} to enhance stability. This study serves as a critical foundation for future ligand design and optimization.

Improving ligand design is essential for developing an early-stage investigational drug that can effectively target the RBD while remaining stable in vitro. Changing the N^{NN} pincer ligand to chelating ligands, such as heterocyclic ligands, can stabilize the ligand–metal bond [24]. However, this modification may prevent the ligand from targeting Y489. A potentially better alternative is to replace the Cu(II) metal ion with a metal ion that offers greater stability while maintaining the desired interactions with Y489. Suitable metal ions could include Co (III), which is highly stable in biological environments [25], or Zn(II), which is redox-inert and biologically relevant.

The water solubility of **Cu1** can be attributed to large solvent-accessible voids present in the crystal. The copper chelate crystallizes as a hexameric metal–organic polymer and the structural basis for this metallocycle formation has been reported [26]. **Cu1** crystallized in the monoclinic space group C2/c with four copper metallocycle hexamers in the unit cell and the asymmetric unit described by three monomers of the hexamer (Figs. S9.1–9.7). As water enters the voids of the crystal, the

molecules disrupt the intramolecular recognition and destabilise the cyclic assembly (Fig. S9.8). The water molecules break intramolecular H-bonds and disrupt van der Waals interactions that stabilise the metallocycle, furthermore, nucleophilic attack of water at the Cu(II) centre may substitute the Cu–$O_{carbonyl}$ bond and break the cyclic coordination pattern. Consequently, there is concomitant release of chelate monomers into solution upon aqua ligand substitution at the Cu(II) centre. The dissolution and monomerization of the hexamers in aqueous media were confirmed by UV–vis spectroscopy and DFT methods (Fig. S9.8).

Metallodrugs have been used for centuries, yet only with modern technology have we gained the ability to elucidate their Mechanism of action This has led to their underrepresentation in preclinical screenings and clinical trials, leaving much of their potential untapped. Notably, metallodrugs exhibit a 10-fold higher hit rate against Enterococcus faecium, Staphylococcus aureus, Klebsiella pneumoniae, Acinetobacter baumannii, Pseudomonas aeruginosa, and Enterobacter species (ESKAPE) pathogens compared to purely organic molecules [27]. In this study, we have demonstrated that leveraging the unique Cu(II) ion with a suitably designed organic ligand allows for the targeted binding (*ca.* $\log K_a = 4.8$) of solvent-exposed tyrosine residues on the CoV RBD. This proof-of-concept study establishes a foundation for developing a new class of universal fusion inhibitors designed to disrupt key biomolecular interactions. The stability limitation of **Cu1** does not negate the fundamental findings of our study. Our results provide valuable insights into the binding properties of **Cu1** and its interaction with the RBD under controlled conditions. Furthermore, our findings confirm that targeting tyrosine residues on the SARS-CoV-2 RBD with copper pincers is viable, and computational models suggest this approach may inhibit viral fusion. These results highlight the potential of metal-based inhibitors and, hopefully, inspire the development of more stable metallodrugs for combating COVID-19 and future pandemics.

CRediT authorship contribution statement

Matthew L. Bracken: Writing – review & editing, Writing – original draft, Visualization, Validation, Resources, Methodology, Investigation, Formal analysis, Data curation, Conceptualization. **Thandeka Moyo-Gwete:** Writing – review & editing, Resources, Methodology, Data curation. **Sheldon Sookai:** Writing – review & editing, Formal analysis. **Frances Ayres:** Supervision, Resources, Methodology, Investigation. **Orde Q. Munro:** Visualization, Supervision, Data curation, Conceptualization.

Declaration of competing interest

The authors declare that they have no known competing financial interests or personal relationships that could have appeared to influence the work reported in this paper.

Acknowledgements

This work was supported by the South African National Institute for Communicable Diseases (NICD) and the South African Research Chairs Initiative of the Department of Science and Innovation (DSI) and National Research Foundation (NRF) of South Africa (Grant No 64799, OQM). The authors thank WITS University and the NRF for funding to purchase a dual-wavelength Bruker D8 Venture X-ray diffractometer (Grant No 129920, OQM). We also thank the Centre for High Performance Computing (Project CHEM1065, CHPC, Cape Town) for access to supercomputing infrastructure.

Appendix A. Supplementary data

Supplementary data to this article can be found online at https://doi.org/10.1016/j.inoche.2025.114887.

Data availability

Data will be made available on request.

References

[1] Timeline: WHO's COVID-19 Response Available online: https://www.who.int/emergencies/diseases/novel-coronavirus-2019/interactive-timeline (accessed on 15 March 2023).
[2] COVID-19 Cases | WHO COVID-19 Dashboard Available online: https://data.who.int/dashboards/covid19/cases (accessed on 23 May 2024).
[3] Islam, N.; Jdanov, D.A.; Shkolnikov, V.M.; Khunti, K.; Kawachi, I.; White, M.; Lewington, S.; Lacey, B. Effects of Covid-19 Pandemic on Life Expectancy and Premature Mortality in 2020: Time Series Analysis in 37 Countries. *bmj* **2021**, *375*.
[4] R. Yadav, J.K. Chaudhary, N. Jain, P.K. Chaudhary, S. Khanra, P. Dhamija, A. Sharma, A. Kumar, S. Handu, Role of Structural and Non-Structural Proteins and Therapeutic Targets of SARS-CoV-2 for COVID-19, Cells 10 (2021) 821.
[5] M. Yuan, N.C. Wu, X. Zhu, C.-C.-D. Lee, R.T.Y. So, H. Lv, C.K.P. Mok, I.A. Wilson, A Highly Conserved Cryptic Epitope in the Receptor Binding Domains of SARS-CoV-2 and SARS-CoV, Science 368 (2020) 630–633, https://doi.org/10.1126/science.abb7269.
[6] J. Lan, J. Ge, J. Yu, S. Shan, H. Zhou, S. Fan, Q. Zhang, X. Shi, Q. Wang, L. Zhang, et al., Structure of the SARS-CoV-2 Spike Receptor-Binding Domain Bound to the ACE2 Receptor, Nature 581 (2020) 215–220, https://doi.org/10.1038/s41586-020-2180-5.
[7] Y. Wang, C. Liu, C. Zhang, Y. Wang, Q. Hong, S. Xu, Z. Li, Y. Yang, Z. Huang, Y. Cong, Structural Basis for SARS-CoV-2 Delta Variant Recognition of ACE2 Receptor and Broadly Neutralizing Antibodies, Nat. Commun. 13 (2022) 871, https://doi.org/10.1038/s41467-022-28528-w.
[8] Q. Geng, K. Shi, G. Ye, W. Zhang, H. Aihara, F. Li, Structural Basis for Human Receptor Recognition by SARS-CoV-2 Omicron Variant BA.1, J. Virol. 96 (2022) e00249–e00322, https://doi.org/10.1128/jvi.00249-22.
[9] F. Li, W. Li, M. Farzan, S.C. Harrison, Structure of SARS Coronavirus Spike Receptor-Binding Domain Complexed with Receptor, Science 309 (2005) 1864–1868, https://doi.org/10.1126/science.1116480.
[10] S. Perlman, Another Decade, another Coronavirus, N. Engl. J. Med. 382 (2020) 760–762, https://doi.org/10.1056/NEJMe2001126.
[11] Y. Chen, X. Zhao, H. Zhou, H. Zhu, S. Jiang, P. Wang, Broadly Neutralizing Antibodies to SARS-CoV-2 and Other Human Coronaviruses, Nat. Rev. Immunol. 23 (2023) 189–199, https://doi.org/10.1038/s41577-022-00784-3.
[12] Y. Zhu, D. Yu, H. Yan, H. Chong, Y. He, Design of Potent Membrane Fusion Inhibitors against SARS-CoV-2, an Emerging Coronavirus with High Fusogenic activity, J. Virol. 94 (2020) e00635–e00720, https://doi.org/10.1128/JVI.00635-20.
[13] S. Mougari, V. Favède, C. Predella, O. Reynard, S. Durand, M. Mazelier, E. Pizzioli, D. Decimo, F.T. Bovier, L.M. Lapsley, et al., Intranasally Administrated Fusion-Inhibitory Lipopeptides Block SARS-CoV-2 Infection in mice and Enable Long-Term protective Immunity, Commun. Biol. 8 (2025) 1–16, https://doi.org/10.1038/s42003-025-07491-4.
[14] C.-K. Siu, Y. Ke, Y. Guo, A.C. Hopkinson, K.M. Siu, Dissociations of copper (II)-Containing Complexes of Aromatic Amino Acids: Radical Cations of Tryptophan, Tyrosine, and Phenylalanine, Phys. Chem. Chem. Phys. 10 (2008) 5908–5918.
[15] T. Kiss, Copper (II) Complexes of Tyrosine-Containing Tripeptides, J. Chem. Soc. Dalton Trans. 1263–1265 (1987).
[16] M. van de Weert, L. Stella, Fluorescence Quenching and Ligand Binding: a critical Discussion of a Popular Methodology, J. Mol. Struct. 998 (2011) 144–150, https://doi.org/10.1016/j.molstruc.2011.05.023.
[17] J. Grzesiak, L. Fellner, K. Grünewald, C. Kölbl, A. Walter, R. Horlacher, F. Duschek, Fluorescence Signatures of SARS-CoV-2 Spike S1 Proteins and a Human ACE-2: Excitation-Emission Maps and Fluorescence Lifetimes, J. Biomed. Opt. 27 (2022), https://doi.org/10.1117/1.JBO.27.5.050501.
[18] A.N. Oldani, J.C. Ferrero, G.A. Pino, Effect of the Intermolecular Hydrogen Bond Conformation on the Structure and Reactivity of the P-Cresol(H2O)(NH3) van Der Waals complex, Phys. Chem. Chem. Phys. 11 (2009) 10409, https://doi.org/10.1039/b916901f.
[19] D. Creed, The photophysics and photochemistry of the near-uv absorbing amino acids-ii. Tyrosine and its simple derivatives, Photochem. Photobiol. 39 (2008) 563–575, https://doi.org/10.1111/j.1751-1097.1984.tb03891.x.
[20] S. Sookai, O.Q. Munro, Complexities of the Interaction of NiII, PdII and PtII Pyrrole-Imine Chelates with Human Serum Albumin**, ChemistryEurope 1 (2023) e202300012, https://doi.org/10.1002/ceur.202300012.
[21] S.M. Kelly, T.J. Jess, N.C. Price, How to Study Proteins by Circular Dichroism, Biochim. Biophys. Acta BBA - Proteins Proteomics 1751 (2005) 119–139, https://doi.org/10.1016/j.bbapap.2005.06.005.
[22] S. Sookai, M.L. Bracken, M. Nowakowska, Spectroscopic and Computational pH Study of NiII and PdII Pyrrole-Imine Chelates with Human Serum Albumin, Molecules 28 (2023) 7466.
[23] J.D. Chodera, D.L. Mobley, Entropy-Enthalpy Compensation: Role and Ramifications in Biomolecular Ligand Recognition and Design, Annu. Rev. Biophys. 42 (2013) 121–142, https://doi.org/10.1146/annurev-biophys-083012-130318.
[24] A.M. Rostas, M. Badea, L.L. Ruta, I.C. Farcasanu, C. Maxim, M.C. Chifiriuc, M. Popa, M. Luca, N. Celan Korosin, R. Cerc Korosec, et al., Copper(II) Complexes

with mixed Heterocycle Ligands as Promising Antibacterial and Antitumor Species, Molecules 25, 3777 (2020) doi:10.3390/molecules25173777.

[25] S.V. Wegner, J.P. Spatz, Cobalt(III) as a Stable and Inert Mediator Ion between NTA and His6-Tagged Proteins, Angew. Chem. Int. Ed. 52 (2013) 7593–7596, https://doi.org/10.1002/anie.201210317.

[26] M.L. Bracken, M.A. Fernandes, D. Wamwangi, O.Q. Munro, Structural Basis for Cu (Ii) Metallocycle Hexamer Formation, New J. Chem. 48 (2024) 8994–8999.

[27] Frei, A.; Zuegg, J.; G. Elliott, A.; Baker, M.; Braese, S.; Brown, C.; Chen, F.; Dowson, C.G.; Dujardin, G.; Jung, N.; et al. Metal Complexes as a Promising Source for New Antibiotics. *Chem. Sci.* **2020**, *11*, 2627–2639, doi:10.1039/C9SC06460E.